Applied Surface Science 711 (2025) 164116

Contents lists available at ScienceDirect

Applied Surface Science

journal homepage: www.elsevier.com/locate/apsusc

Full Length Article

Understanding the interfacial changes of $PtCo_3O_4$ catalysts during the dehydrogenation of ammonia borane

Silvio Bellomi [a], Daniel C. Cano-Blanco [b,c], Yaning Han [d], Juan J. Delgado [d], Xiaowei Chen [d], Kirill A. Lomachenko [f], Ilaria Barlocco [a], Davide Ferri [b], Alberto Roldan [e], Alberto Villa [a,*]

[a] Dipartimento di Chimica, Università degli Studi di Milano, via Golgi 19, I-20133 Milano, Italy
[b] Paul Scherrer Institute, PSI Center for Energy and Environmental Sciences, CH-5232 Villigen PSI, Switzerland
[c] École polytechnique fédérale de Lausanne (EPFL), 1015 Lausanne, Switzerland
[d] Departamento de Ciencia de los Materiales, Ingeniería Metalúrgica y Química Inorgánica, Facultad de Ciencias, Universidad de Cádiz, Campus Río San Pedro, Puerto Real (Cádiz) E-11510, Spain
[e] Cardiff Catalysis Institute, School of Chemistry, Cardiff University, Main Building, Park Place, CF10 3AT Cardiff, United Kingdom
[f] European Synchrotron Radiation Facility, 71 avenue des Martyrs, CS 40220, 38043 Grenoble Cedex 9, France

ARTICLE INFO

Keywords:
Ammonia borane
Metal-support interaction
Catalytic interface
Hydrogen
DFT

ABSTRACT

The redox properties of oxides are critical in catalysis and can be modified at the interface between oxides and metals; as a consequence, working catalysts can be reconstructed. Herein, the influence of metal-support interactions on the interface between Pt and Co_3O_4 was disclosed during the batch ammonia borane decomposition. Co_3O_4 with and without decorating Pt were compared, and tested against Pt on a non-reducible oxide ($PtAl_2O_3$). The kinetic profiles were analysed using kinetic models, and both fresh and used samples were characterised using XRD, XPS, XAS, HR-TEM, CO adsorption by IR, and *in situ* ATR-IR. The combined study revealed an enhanced reaction rate for $PtCo_3O_4$ and its reconstruction under reaction conditions due to metal-support interaction, and disclosed the nature of the stable active sites formed under reaction conditions. Indeed, during the reaction, metallic Pt re-distributed, and the H-spillover to the support reduced the surface of Co_3O_4, leading to Pt clusters on Co(II)-enriched Co_3O_4. Atomic-scale insights on the surface redox properties of the catalysts were then obtained through DFT, and the modification of $PtCo_3O_4$ was attributed to the facile reduction of octahedral Co(III) ions at the metal/oxide interface, and rationalised as a consequence of charge transfer from Pt to Co_3O_4.

1. Introduction

The properties of solid surfaces are the result of an ensemble of ions and oxidation states [1,2]. For instance, the redox character of metal oxides is essential in determining their activity in catalysis, and the deposit of dopants, i.e. metal nanoparticles, induces substantial modification, deeply influencing the catalytic performance [3–6]. The profound impact of metal-oxide interfaces on the performance of catalysts was demonstrated for several chemical reactions performed in the gas phase, including CO oxidation [7,8], steam reforming [9], and alcohol oxidation [10]. These interfaces were also found to be beneficial in liquid-phase dehydrogenation reactions, chemical processes of utmost interest to the actual scientific community, including formic acid [11], hydrazine [12–14], and ammonia borane [15–17].

In this context, ammonia borane is one of the most widely investigated hydrogen vectors, due to its high hydrogen capacity (19.6 wt%) and controlled release of H_2 under mild conditions, Eq. (1) [18–22].

$$NH_3BH_3 + 2H_2O \rightarrow NH_4BO_2 + 3H_2 \quad (1)$$

For this reaction, the combination of Pt and Co_3O_4 is recognised as optimal, and the catalysts demonstrated excellent activity and stability due to the peculiar metal-oxide interface, which induces a dual-function interfacial mechanism [17,23–25]. The Pt sites effectively promote dehydrogenation, leading the H adatoms to diffuse and spill onto the reducible Co_3O_4 [3,26–28]. The reducible oxide establishes a steady state between generating oxygen vacancies and replenishing them

* Corresponding author.
E-mail address: alberto.villa@unimi.it (A. Villa).

https://doi.org/10.1016/j.apsusc.2025.164116
Received 22 May 2025; Received in revised form 26 June 2025; Accepted 20 July 2025
Available online 21 July 2025

through water dissociation. Hydrogen adatoms recombine and evolve as H_2 at the metal-oxide interface [25].

Atomic-level resolution of the ammonia borane decomposition and the nature of the active sites is not trivial on the spinel structure of Co_3O_4, as its surface exposes octahedral Co(III) and tetrahedral Co(II) ions. To this end, information on the catalytic active sites can be indirectly obtained by applying kinetic models to the hydrogen evolution profiles. The kinetic theory of Finke-Watzky (FW) describes the structural transformations that a catalyst undergoes during processes involving the production/consumption of hydrogen [29]. The method was initially developed to describe the nucleation and growth of clusters in solution in the presence of H_2 [29–31]. If the rate of the probe reaction is sufficiently high, sigmoidal-shaped H_2 evolution profiles are obtained, which allow an indirect quantitative determination of structural changes [16,17,29]. Over the years, the FW model was also applied to metal nanoparticles supported on transition metal oxides [15,17], and the general scheme was extended to describe the transformation of a pre-catalyst under reducing conditions [29–31]. Successful examples of the application of the FW model to kinetic profiles were also reported for the ammonia borane dehydrogenation on supported catalysts, including $PtCo_3O_4$ [15–17,25]. However, the reactive role of the metal/oxide interface during the ammonia borane dehydrogenation and the modifications induced on the materials by the substrate have never been clarified in detail.

This work provides insights into the behaviour of the metal/oxide interface between dispersed Pt and Co_3O_4 during the ammonia borane dehydrogenation, the restructuring occurring *in-situ*, and the nature of the active sites. $PtCo_3O_4$ was tested and compared to the pristine oxide and a non-reducible oxide ($PtAl_2O_3$) [32,33]. The analysis of the catalytic profiles with kinetic models, a thorough catalyst characterisation, and atomistic modelling based on density functional theory provided key insights into the surface redox properties. Uniquely due to MSIs, the entire metal/oxide interface is restructured by the reactive interaction with ammonia borane due to H spillover, and the highly active and stable phase on $PtCo_3O_4$ is formed – Pt clusters on Co(II)-enriched Co_3O_4.

2. Methods

2.1. Materials

Ammonia borane (AB, 90 %), cobalt (II) nitrate hexahydrate ($Co(NO_3)_2{\cdot}6H_2O$, 98 %), sodium carbonate (Na_2CO_3, ≥98 %) and Pt (II) chloride (H_2PtCl_6, 99.999 %) were obtained from Sigma-Aldrich and used without further purification.

2.2. Catalyst synthesis

Co_3O_4 was prepared by a rate-controlled co-precipitation method with a Na_2CO_3 as previously reported [34]. In a typical preparation, the nitrate precursor, $Co(NO_3)_2{\cdot}6H_2O$, was dissolved in the desired volume of Milli-Q water (50 mL/g catalyst) and stirred at 800 rpm for 30 min. Na_2CO_3 (1 M) was added with a peristaltic pump at a rate of 2 mL/min until pH = 8.5 was reached, which was monitored continuously with an immersion pH electrode. The precipitate was aged at room temperature for 3 h, then washed with hot purified water. The precipitate was dried at 373 K overnight and calcined in a muffle furnace at 773 K (2 K/min) for 4 h, providing the sample labelled as Co_3O_4. The desired amount of Pt (H_2PtCl_6) was deposited by incipient wetness impregnation to achieve a metal loading of 1 wt%, and then calcined at 773 K (2 K/min) for 4 h to favour the metal redispersion and enhance the metal-support interactions, labelled as $PtCo_3O_4$. A similar procedure was employed to synthesise the $PtAl_2O_3$ used as a reference, which was previously reported elsewhere [33].

2.3. Catalytic activity

The hydrolytic dehydrogenation of ammonia borane (AB) was performed in a 27 mL two-necked round-bottom flask at a constant reaction temperature of 303 K. H_2 evolution was monitored by measuring the partial pressures of the released product using the Man On The Moon X104 kit [35,36]. Typically, the catalyst (AB/Pt molar ratio 500/1) was added to the reactor containing 5.0 mL of distilled water and heated to the desired temperature. Finally, 0.25 mmol of AB was injected into the final mixture under stirring (1400 rpm). The kinetic profiles were collected with a 2 Hz frequency (0.5 point/s) until reaction completion, which was indicated by a pressure plateau. All the tests were performed three times to ensure experimental reproducibility and assess measurement uncertainty.

2.4. Characterization

X-ray diffraction patterns were collected on a D8 ADVANCE diffractometer (Bruker) using Cu Kα1 radiation (λ = 1.5406 Å). Data were recorded from 20° to 70° 2θ at a step size of 0.02°/s.

High-angle annular dark-field scanning transmission electron microscopy (HAADF-STEM) characterization of the samples was conducted using a TEM/STEM FEI Talos F200X G2 microscope (Thermo Fisher Scientific, Waltham, MA, USA). This advanced equipment enables the acquisition of HAADF-STEM images and Energy-dispersive X-ray spectroscopy (XEDS) maps using its 4 Super-X SDDs. HAADF-STEM is an atomic number-sensitive technique that allows the identification of small nanoparticles of elements with high atomic numbers, such as Pt, on the surface of nanoparticles with lower atomic numbers, like Co. Elemental maps were obtained with a beam current of approximately 90 pA and a dwell time of 75 μs.

Co K-edge XAS data were collected at the BM23 beamline of the European Synchrotron Radiation Facility (ESRF) [37]. The storage ring was operating in the uniform mode with 200 mA current. The beam was monochromatized by a fixed-exit double-crystal monochromator (Si111 crystals) designed in the ESRF. Higher harmonics were removed by a pair of flat Si mirrors positioned at 3 mrad. The measurements were conducted in transmission geometry using continuous scanning mode. Incident and transmitted X-rays were detected by gas-filled ionization chambers. X-ray absorption near edge structure (XANES) processing and extended X-ray absorption fine structure (EXAFS) analysis were performed using the Athena and Artemis software from the Demeter suite [38]. Data fitting of the EXAFS function of the Co–K edge in *R* space between 1 and 3.5 Å, and k-range of 3–14 $Å^{-1}$, using cobalt-oxygen (Co–O), cobalt-cobalt octahedral (Co-Co(Oh)), cobalt-cobalt tetrahedral (Co–Co(Td)) scattering paths. The amplitude factor of the EXAFS equation ($S_0^2 = 0.736$) was obtained from the fit of a Co reference and fixed for all the samples.

In situ diffuse reflectance infrared Fourier transform (DRIFT) spectra of CO adsorption were obtained using a Vertex 80 spectrometer (Bruker) equipped with a mercury cadmium telluride (MCT) detector. Typically, the solid sample was first positioned on the top of several stacked stainless steel meshes in a high-temperature reaction cell (Harrick) fitted with KBr windows, and then this DRIFT cell was installed inside the Praying Mantis (Harrick), which is located in the sample compartment of the spectrometer. The temperature of the catalyst was maintained at 308 K and pure He was continuously purged through the bottom of the catalyst bed for 60 min to remove the adsorbed water. In addition, a cold trap of a mixture of liquid nitrogen and 2-propanol at 184 K was used to eliminate water present in the gas line before entering the DRIFTS cell. After that, a mixture of 1 vol% CO/He was introduced into the reaction cell with a total flow rate of 100 mL/min, and the spectra were collected at different times within 20 min. Finally, the pure He was introduced again for 20 min to remove the gas phase and weakly adsorbed CO. Before the measurement, the reference spectrum without sample was recorded at room temperature using an aluminum foil. DRIFT spectra

were recorded with 64 scans, ranging from 4000 to 600 cm^{-1} with a resolution of 4 cm^{-1}.

In situ infrared spectroscopy experiments in attenuated total reflection mode (ATR-IR) were performed using a Vertex v70 (Bruker) spectrometer equipped with a liquid-nitrogen-cooled MCT detector, a mirror unit and a homemade cell [39]. The parallelogram ZnSe prism (45°, 34 mm × 20 mm × 2 mm; Crystran Ltd.) was coated with a powder layer obtained from the evaporation of an aqueous slurry of the catalyst (5 mg/mL H_2O). Solutions and neat solvents were provided from independent glass bottles at a flow rate of 0.3 mL min^{-1} using a peristaltic pump (Reglo 100, Ismatec). A 4-ports valve (Cheminert, VICI) enabled fast switching between two different solutions at the cell inlet. The switch system was synchronised to the spectra acquisition using the OPUS software (Bruker). The experiments were carried out in flow to increase the control over the reactive environment, preventing the accumulation of surface species [40,41]. In a typical procedure, the solutions were degassed in bubbling Ar for 30 min. After mounting the coated crystal in the cell body, the temperature was adjusted to 303 K while equilibrating the catalyst layer in H_2O for 30 min. At this point, a background spectrum was collected, followed by a 30-min equilibration in the presence of the AB solution (5 mM). Finally, a modulated excitation (ME) experiment was started that consisted of the admittance of the first solution into the cell for 125 s, followed by the switch to the second solution for the same amount of time (modulation period, 250 s), a sequence that was repeated ten times. Spectra were collected continuously by averaging 10 scans at a scanner velocity of 80 kHz and a spectral resolution of 4 cm^{-1}, resulting in a time resolution of 1.25 s/spectrum. Only the periods at the quasi-stationary regime were averaged to improve the S/N ratio, and signal enhancement was achieved by phase-sensitive detection (PSD) analysis using a Matlab script that provides phase-domain spectra [42].

2.5. Computational methods

Spin-polarized periodic plane-wave DFT calculations were carried out using the Vienna Ab-initio Simulation Package (VASP) [43]. Projected augmented wave potentials with PBE functionals were employed, using a cutoff to the kinetic energy of 400 eV for the expansion of the plane-wave basis set [44,45]. The optimisation thresholds for electronic energies and ionic forces relaxation were 10^{-5} eV and 0.01 eV/Å, respectively. The Brillouin zone was sampled using a 8 × 8 × 8 Γ-centred k-point mesh generated through the Monkhorst–Pack method, minimising any Pulay stress [46]. The localisation and strong on-site Coulomb repulsion of Co 3d-states was addressed using DFT + U in the rotationally invariant Dudarev scheme [47] with the Hubbard parameter of 3.3 eV [48,49]. Ionic positions, lattice parameters, and electronic structure of the bulk systems were analysed to validate the accuracy of the computational setup employed (Fig. S1 and Table S1). We employed the Atomic Simulation Environment (ASE) to generate the Co_3O_4 (1 1 0) slab model from the optimised bulk system (ICSD-36256) [50]. The (1 1 0) crystal face was reported experimentally and proven effective in reproducing the redox properties of Co_3O_4 and in different catalytic processes [51–53]. Two types of surface terminations are possible for the Co_3O_4 (1 1 0) spinel surface [53]. In agreement with previous reports, the Co_3O_4 (1 1 0) employed exposes two fourfold coordinated (Co_{Oct}) cations in octahedral sites, two twofold coordinated (O^{2c}) and two threefold coordinated (O^{3c}) oxygen sites in the outermost surface [53,54]. The O^{2c} anions are bonded to one fourfold coordinated cation (Co_{Td}) and one Co_{Oh} cation, whereas O^{3c} has three Co_{Oh} nearest neighbours. Non-stoichiometric slab terminations correct the unphysical dipole moment perpendicular to the surface and converge the surface properties [55,56]. We employed a 7-atomic-layer slab, in which atoms in the central layer were fixed to the bulk positions while fully relaxing the other six layers, three for each side of the slab [52,53]. A vacuum of 16 Å was created along the z-axis to form the surfaces and avoid any interaction between adjacent images. The convergence criteria were kept the same as in the bulk calculations, yet the k-points adapted to a 2 × 2 × 1 grid. Binding energies (E_b) were calculated using Eq. (2). Where E_A and E_B are the energies of the isolated species, while E_{AB} refers to the combined system.

$$E_b = E_{AB}\text{-}E_A\text{-}E_B \quad (2)$$

2.5.1. Optimization of $PtCo_3O_4$

A metal-cluster model simulating the experimentally observed size is prohibitively expensive to compute using electronic structure methods. Nonetheless, simplified computational models complement experiments with atomic-level insights. Considering the large number of atoms present in the structures, a Pt_8 cluster was employed to compromise the representativeness and computational effort of the models [13,57]. The current choice for eight atoms in the cluster is pragmatic. It is based on a large enough atomic population to resemble the local atomic environment of a metal nanoparticle and capture the metal-support interaction realistically, but with a size small enough to allow an extensive mapping of energy and morphology among its configurations. An unbiased genetic algorithm (GA) generated about 200 structures, which were evaluated using spin-polarized DFT + U energies (GA-sDFT + U). This methodology provided a putative global minimum of the clusters supported on the Co_3O_4 (1 1 0) slab. The GA involved a pool of 8 members with crossover and mutation operations procedures within a randomisation and displacement operators framework. The initial pool members were randomly generated with a cluster-to-surface height of 2.0 Å. A mutation rate of 10 % was employed to guarantee the generational variety among the structures [58].

The energy of all these structures was determined using a soft optimisation protocol in VASP, i.e., thresholds for electronic and ionic relaxation energies, respectively, of 10^{-4} eV and 10^{-3} eV, evaluated at the Γ-point and with frozen supports. An increased number of initial non-self-consistent steps and linear mixing involving the metal d-orbitals improved the wavefunction convergence. The Brillouin-zone evaluation was eased using the Gaussian method with a smearing width of 0.05 eV [59]. The putative global minimum of Pt_8 was then re-optimised at an electronic and ionic relaxation forces threshold of 10^{-5} eV and 0.02 eV/Å, using a k-points grid of 2 × 2 × 1. On the slab models, the thermodynamic energy barrier for the formation of an oxygen vacancy ($E_f(O)$) was calculated as the difference between the total energy of defective (E_{def}) and pristine (E_p) surfaces, using 1/2 of the O_2 molecule energy in the gas phase as reference, Eq. (3). In all cases, after the introduction of the surface defect, the uppermost slab layers were allowed to relax, as well as the metal cluster, if present.

$$E_f(O) = E_{def}\text{-}E_p + \frac{1}{2}E(O_2) \quad (3)$$

3. Results and discussion

3.1. Catalytic activity

Metal/oxide interfaces modify the local properties of oxide surfaces *via* metal support interactions (MSIs) [3]. Here, cobalt oxide (Co_3O_4) was impregnated with 1 wt% of Pt ($PtCo_3O_4$), and the performance for the ammonia borane hydrolysis compared to that of the bare Co_3O_4 (reducible oxide) and a $PtAl_2O_3$ (non-reducible oxide) catalyst to disclose the role of MSIs. As shown in Fig. 1a, the reaction on $PtAl_2O_3$ started immediately and plateaued in 20 min, i.e. reaction completion. Differently, on $PtCo_3O_4$ the hydrogen evolution followed a sigmoidal shape. After a short time of about 1 min (induction period), the hydrogen generation abruptly increased, and the reaction was completed in 5 min. On both materials, a comparable number of hydrogen moles was obtained, respectively 0.76 and 0.78 mmol for Pt on Al_2O_3 and Co_3O_4, and close to the theoretical value of 0.81 mmol, confirming the mechanism of hydrolytic dehydrogenation [17,25]. The catalytic activity was calculated by taking the slope of the profiles at 50

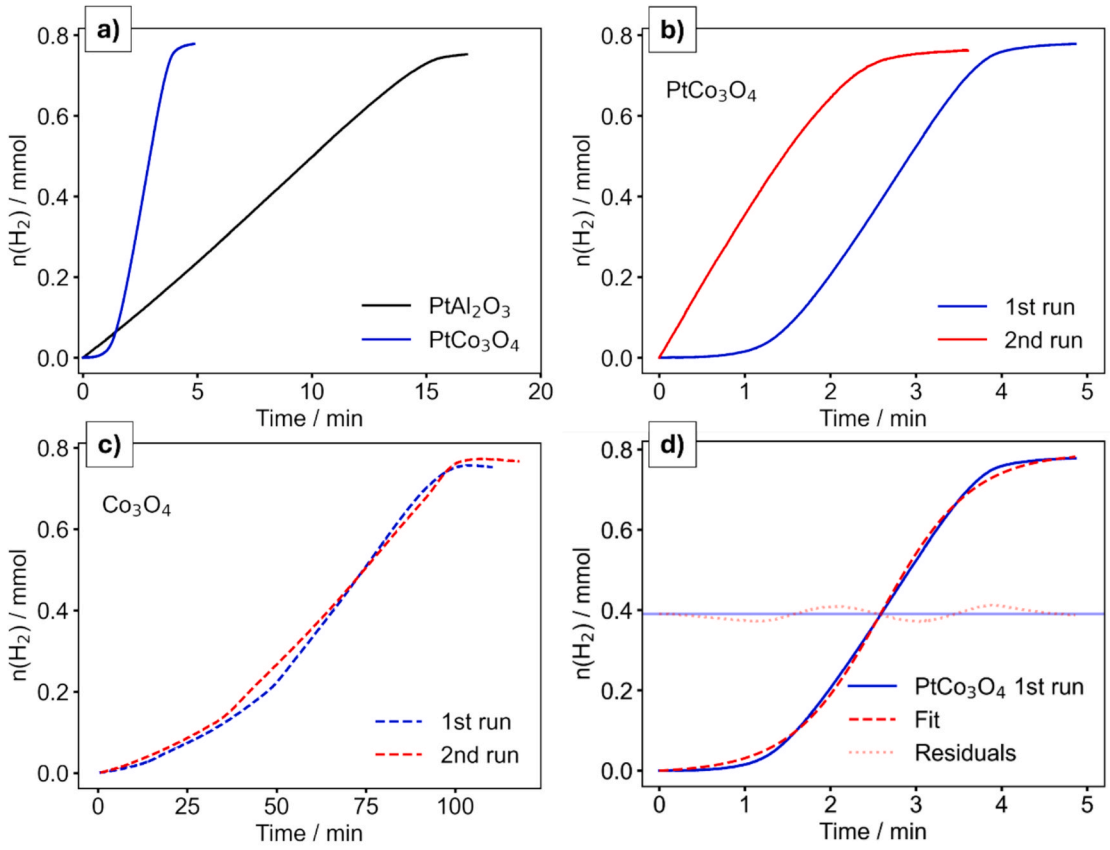

Fig. 1. Kinetic profiles for the ammonia dehydrogenation reaction on a) $PtAl_2O_3$ (black) and Pt/Co_3O_4 (blue). Repeated reaction runs on b) $PtCo_3O_4$ and c) Co_3O_4. d) Non-linear least squares fit of the sigmoidal kinetic profile of $PtCo_3O_4$ with the Finke-Watzky kinetic mechanism. All the experiments were performed at 303 K and 1400 rpm, with 0.27 mmol of ammonia borane in 5 mL of distilled H_2O.

% of the overall hydrogen production, i.e., regime of linear evolution, therefore excluding any induction time from the calculation (Section S1.1) [17]. Compared to $PtAl_2O_3$ (199 min^{-1}), Pt dispersed on Co_3O_4 exhibited a fourfold activity value (804 min^{-1}), clearly indicating that the redox properties of the oxides and MSIs influence the reaction rate and the catalyst performance.

The induction time observed during the hydrogen evolution on $PtCo_3O_4$ could indicate the occurrence of structural changes during the reaction [29–31]. Hence, to confirm that, the profiles were analysed *via* a Finke-Watzky kinetic model, a scheme used to describe the transformation of a meta-stable catalyst state A to a state B, under reducing conditions [17,29,31]. In good agreement with the literature [29,60], the profile of $PtCo_3O_4$ was well fit (Fig. 1b, Section S1.2 for the detailed method, results of the fit and a discussion of the model), supporting a correlation between the sigmoidal profile of $PtCo_3O_4$ and modifications of the oxide properties by Pt deposition [29,60]. To explore whether further changes can be induced by exposure to the AB solution, a second reaction run was performed on the same portion of the catalysts. Fig. 1c shows the results for $PtCo_3O_4$. The disappearance of the firstly observed induction period, and the comparable catalytic activity values (804–825 min^{-1}, Fig. S2), were taken as evidence of the stability of the *in-situ* formed active phase. On the other hand, the absence of differences in the profiles of $PtAl_2O_3$ excluded any significant modification of the material induced by the reaction, Fig. S3.

Lastly, the role of Pt in determining such transformations was highlighted through the comparison of bare and Pt-modified Co_3O_4, Fig. 1d. Here, no notable difference in the profiles was observed between the subsequent runs, and none of the kinetics of Co_3O_4 was well fit with the FW model (Fig. S4). These results suggested that no change occurred in the presence of only Co_3O_4, and confirmed that dispersed Pt is responsible for the induced structural changes.

3.2. *Characterisation of the $PtCo_3O_4$ interface*

The comparison between $PtCo_3O_4$, $PtAl_2O_3$, and Co_3O_4, and the use of the FW kinetic model suggested a modification of the reducible oxide (Co_3O_4) under reaction conditions, only in the presence of Pt ($PtCo_3O_4$). Hence, we performed *in situ* ATR-IR to study the origin of the induction period of Fig. 1a and assign it to possible structural changes induced by the surface reaction mechanism of AB [61,62]. The exposure of the catalyst to an aqueous solution of AB caused an upward shift of the baseline (Fig. 2a), often observed when electron transfer occurs [39]. A surface reduction of Co_3O_4 lowers the refractive index of the catalyst and causes an increase in the absorption, i.e., the penetration depth is extended and more catalyst layer (less contacted solution) is probed [61,63]. Hence, the shift was explained in terms of charge transfer to the surface of Co_3O_4, causing reduction, which was proven irreversible upon exposure of the catalyst to a neat and an O_2-saturated water solution, each for 30 min [39].

Together with the baseline changes, the appearance of different signals in the 2000–1000 cm^{-1} range occurred, a region that corresponds to the signal characteristics of the species involved in the AB dehydrogenation. The AB (NH_3BH_3) dehydrogenation proceeds through the breakage of B-H bonds and the formation of (meta-)boric acids (BAc, NH_4BO_2), Eq. (1). AB possess characteristic peaks at 2330 (γ B–H), 1605 (δ N–H) and 1175 (δ B–H) cm^{-1}, while BAc can be distinguished through the peaks at 1402 (δ B–O), 1227 (δ B–O), 970 (ρ B–O) cm^{-1} [64]. Hence, to correlate the changes observed with the surface reaction mechanism of the AB hydrolysis, pulsed experiments consisting of alternating water and aqueous AB solutions were performed. As shown in Fig. 2b, a

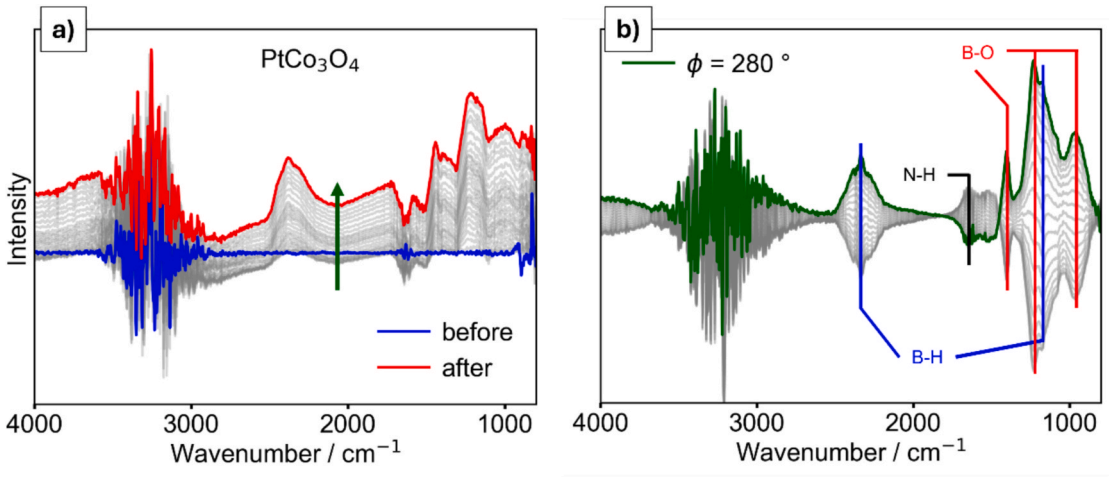

Fig. 2. (a) In situ ATR-IR spectra of $PtCo_3O_4$ during AB exposure for 30 min, and d) phase-resolved spectra obtained from PSD of the time-resolved spectra collected during the pulsed experiment. The spectrum at phase angle $\phi = 280°$ is marked to guide the eye.

periodic modulation in the surface signal of B-H (AB) and B-O (BAc) species was observed, while no clear variation was observed for the N–H of AB. This confirms the role of surface [–BH_3] species as the H source [24,25,65], and was taken as evidence of the AB dehydrogenation proceeding through the breakage of B–H bonds, with the formation of BAc species. On $PtCo_3O_4$ catalysts, the B-H breakage occurs on the Pt particles, and H spills and recombines to H_2 on Co_3O_4 [25]. Therefore, we assigned the irreversible baseline changes to the spillover of H atoms derived from the breakage of the B-H bonds, reducing the support [39].

The kinetic data of $PtCo_3O_4$ interpreted *via* the FW theory, complemented by the ATR-IR experiments, indicated changes in the material occurring *in-situ* due to the interaction with AB and spillover of H species, pointing to an irreversible surface reduction of Co_3O_4. To correlate this information with the surface composition and atomicity, $PtCo_3O_4$ before and after the reaction was characterised through XPS and CO-DRIFTS, Fig. 3a-b.

The XPS results are summarised in Table S2. In agreement with the literature, the Co *2p* XPS narrow scan of Co_3O_4 is a spin–orbit doublet composed of signals related to Co(III) (779.6 eV) and Co(II) ions (780.9 eV), and a less intense satellite structure at ca. 10 eV from the main

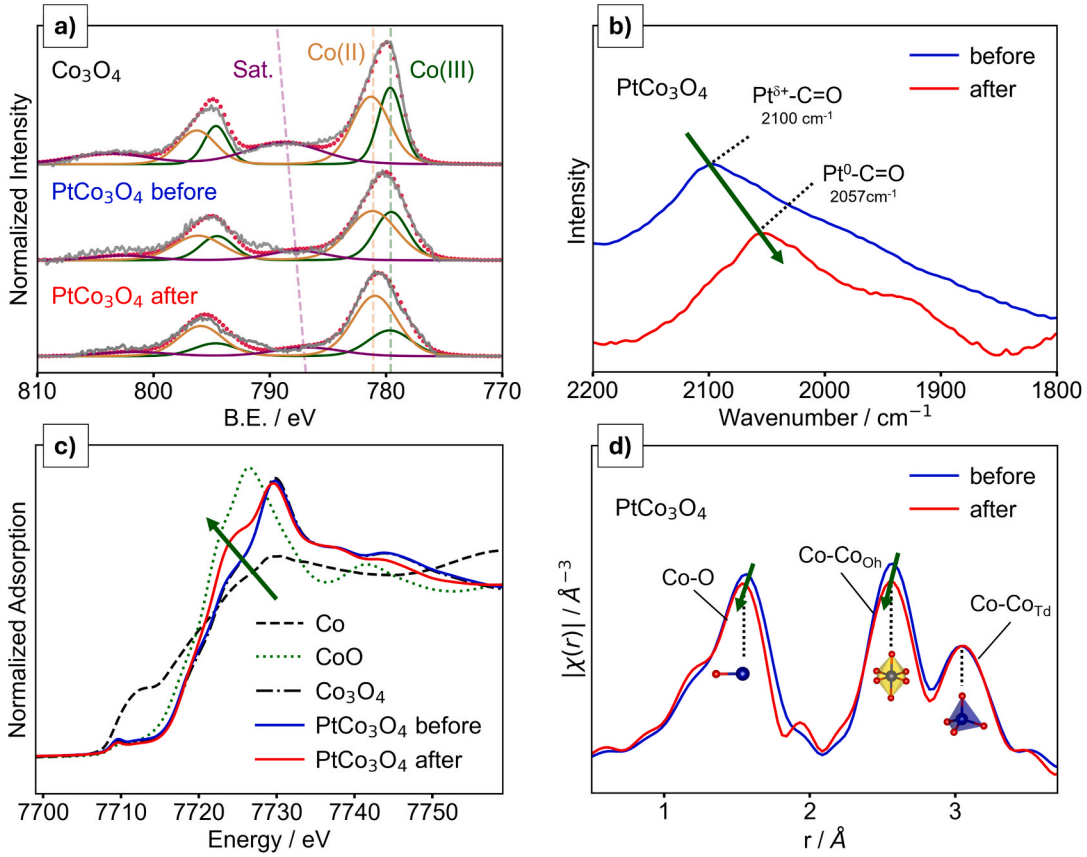

Fig. 3. Characterization of $PtCo_3O_4$, before and after the reaction. a) Co 2p HR-XPS, b) CO-DRIFT spectra over the $PtCo_3O_4$ catalyst after 20 min of CO adsorption and 20 min of a He flow at 308 K, c) Co K-edge XANES and d) k^2-weighted phase-uncorrected FT-EXAFS.

photoemission line [28]. For the as-synthesised Co_3O_4 sample (Fig. 3a), the Co(III)/Co(II) ratio of 0.82 and the satellite position at 788.7 eV are in line with the literature results reported for a normal spinel structure [28]. After the deposition of Pt, the Co(III)/Co(II) ratio decreased from 0.83 to 0.67, and the satellite shifted by ca. 1 eV towards the main peak, suggesting a diminished exposure of Co(III) species and soft reduction of the Co_3O_4 surface. After the reaction on $PtCo_3O_4$, the XPS Co(III)/Co(II) ratio decreased from 0.67 to 0.35 (Fig. 3a), and an additional shift of the satellite by ca. 1 eV occurred, indicating a deeper reduction of surface Co (III) ions. The Pt signal was not analysed due to the surface content of exposed Pt close to the limit of instrumental detection, preventing any reliable conclusion (Table S2). However, we obtained complementary information on the oxidation state of exposed Pt through CO-DRIFTS (Fig. 3b). In accordance with the XPS data, the sample before the reaction showed the signal of CO coordinated to partially positively charged Pt species ($Pt^{\delta+}$ 2100 $cm^{-}1$). $PtAl_2O_3$ was analysed as a reference to obtain information on the oxidation state of Pt on a non-reducible oxide, i.e., excluding MSIs. The complete characterisation is reported elsewhere [33]. Here, the same experiment on the material before any reaction showed a signal at 2056 cm^{-1} [33], corresponding to well-dispersed metallic Pt particles. It is worth noting that no CO adsorption band was observed on pure Co_3O_4. Hence, the surface analysis of the catalysts before any reaction confirmed the absence of a significant Pt-support interaction when Al_2O_3 is used, while the use of a reducible support such as Co_3O_4 induced a net transfer of charge between the components ($Pt^{\delta+}Co_3^{\delta-}O_4$). After the reaction on $PtCo_3O_4$, a conversion of the $Pt^{\delta+}$ sites to Pt^0 occurred, and ν(CO) shifted from 2100 to 2057 cm^{-1}, Fig. 3b. This modification of Pt corroborates the surface reduction of $PtCo_3O_4$ observed during ATR-IR and confirmed by XPS, and points to a restructuring of the catalyst surface under reaction conditions due to MSIs.

Therefore, we investigated the impact of the cobalt oxide reduction through XAS of $PtCo_3O_4$ before and after the reaction. As shown in Fig. 3c, the Co K-edge XANES of $PtCo_3O_4$ is in perfect line-to-line correspondence with that of Co_3O_4. This, in combination with the surface information from XPS, supports the absence of changes in the oxidation state of bulk Co_3O_4 due to the insertion of Pt, and limits the transfer of charge to the uppermost surface layers in closer contact with the metal. On the other hand, after the reaction, the absorption edge of $PtCo_3O_4$ shifted to lower energies and broadened, indicating an extended reduction and mixed valence of bulk Co_3O_4 [25,66–68]. The XANES features were supported by a quantitative analysis of the FT-EXAFS, Fig. 3d, as the same comparison showed a modification in the distribution of the Co sites. The best parameters and the corresponding fit of the signals in R and k-space are shown in Table S3 and Fig. S5, respectively. In a normal spinel structure, Co(III) and Co(II) are positioned at octahedral (Co_{Oh}) and tetrahedral (Co_{Td}) sites, respectively [28], and a variation of their relative population affects the redox properties of Co_3O_4 [67,69]. Indeed, after the reaction, the coordination number (N) of octahedral Co sites (N_{Oh}) decreased compared to that of the tetrahedral ones (N_{Td}), N_{Oh}/N_{Td} shifted from 0.88 to 0.73, with a diminished Co-O coordination, 4.5 to 3.9 (±0.2). To support this data, an alternative model fixing N_{Td} between the $PtCo_3O_4$ sample before and after the reaction was also used, and similar results were obtained (Table S3, Fig. S5), confirming the modification of the octahedral sites as the responsible for the changes observed.

The FT-EXAFS indicated a reduction of Co_3O_4 and changes of the local structure, and confirmed the surface modifications observed from the previous characterisations. Therefore, changes in the long-range ordering and crystal structure of Co_3O_4 were evaluated through XRD, Fig. 4. The pattern of Co_3O_4 exhibited peaks at 2θ values of 19.1, 31.4, 37.0, 38.7, 45.0, 55.9, 59.6 and 65.6°, which are the characteristics (111), (220), (311), (222), (400), (422), (511) and (440) planes of the normal spinel structure (Fd3m) [28]. The spinel structure was preserved in $PtCo_3O_4$, and no signal of Pt was observed even after interaction with AB, indicating a fine dispersion on the support [70]. Then,

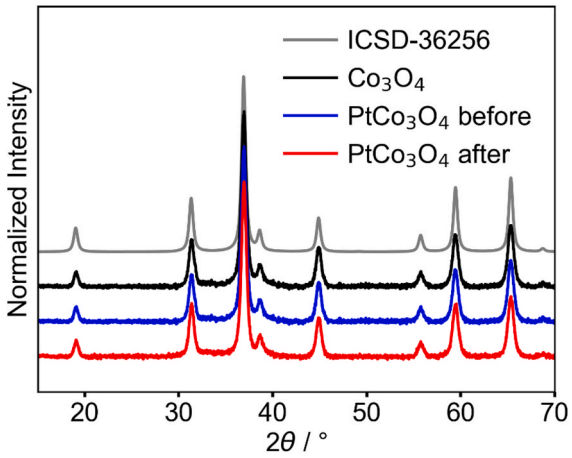

Fig. 4. XRD patterns of the catalysts.

STEM-HAADF was used to obtain insights into the structural and compositional features, Fig. 5. Pt can be easily distinguished on the Co surface in the HAADF images due to its higher atomic number, which results in greater contrast compared to Co. This visual distinction is further corroborated by the EDS mapping, which confirms the spatial distribution of Pt on the Co matrix. In the material before the reaction, well-dispersed small Pt clusters ranging from 0.5 to 1 nm were observed. In contrast, the used sample revealed larger (1.5–4 nm) Pt nanoparticles, indicating the agglomeration of Pt during the reaction. Additionally, the EDS data for the fresh sample showed the presence of residual chlorine species, originating from the platinum precursor used during synthesis, which were completely removed by the reaction with AB. The insights on the Pt morphology were found in agreement with the information on the oxidation state of Pt obtained from CO-DRIFTS.

Overall, the reaction of $PtCo_3O_4$ with AB generated the catalyst active phase – Pt clusters on Co(II)-enriched Co_3O_4. The thorough characterisation pointed to surface modifications and excluded significant changes in the long range ordering and crystal structure of Co_3O_4. Therefore, DFT simulations of Pt clusters supported on Co_3O_4 were employed to obtain atomistic insights into the role of the metal/oxide interface in such changes.

3.3. *Modelling of the $PtCo_3O_4$ interface*

The redox properties of Co_3O_4 in the presence and absence of Pt clusters were investigated at the spin-polarised DFT-PBE + U level using the formation of oxygen vacancies, a standard descriptor for the reducibility of an oxide [3]. Schematically represented in Fig. 6a-b, the Co_3O_4 structure is a normal spinel, i.e., Co(III) and Co(II) are respectively positioned at octahedral (Co_{Oct}) and tetrahedral (Co_{Td}) sites [28]. The reconstructed Co_3O_4 (1 1 0) slab model with no dipole perpendicular to the surface exposes, on the outermost layer, 2 four-fold coordinated Co_{Oct}, 2 two-fold coordinated (O^{2c}), and 2 three-fold coordinated (O^{3c}) oxygen sites [28]. Fig. 6b shows the putative minimum configuration of the Pt cluster, obtained through a global optimisation procedure balancing the computational feasibility of the calculations and their physical validity [13,57]. It should be made clear that the computational models used here are a simplification of real powder catalysts, not aimed at quantitatively reproducing the surface chemistry of the catalyst, but rather at qualitatively illustrating the surface phenomena existing on these materials and the fundamental interaction between the components of the metal/oxide interface. Consequently, the study was limited to investigating surface properties without discussing their direct impact on the catalysis.

The presence of MSIs in $PtCo_3O_4$ was probed by analysing the interaction between the cluster and the support. The exothermic

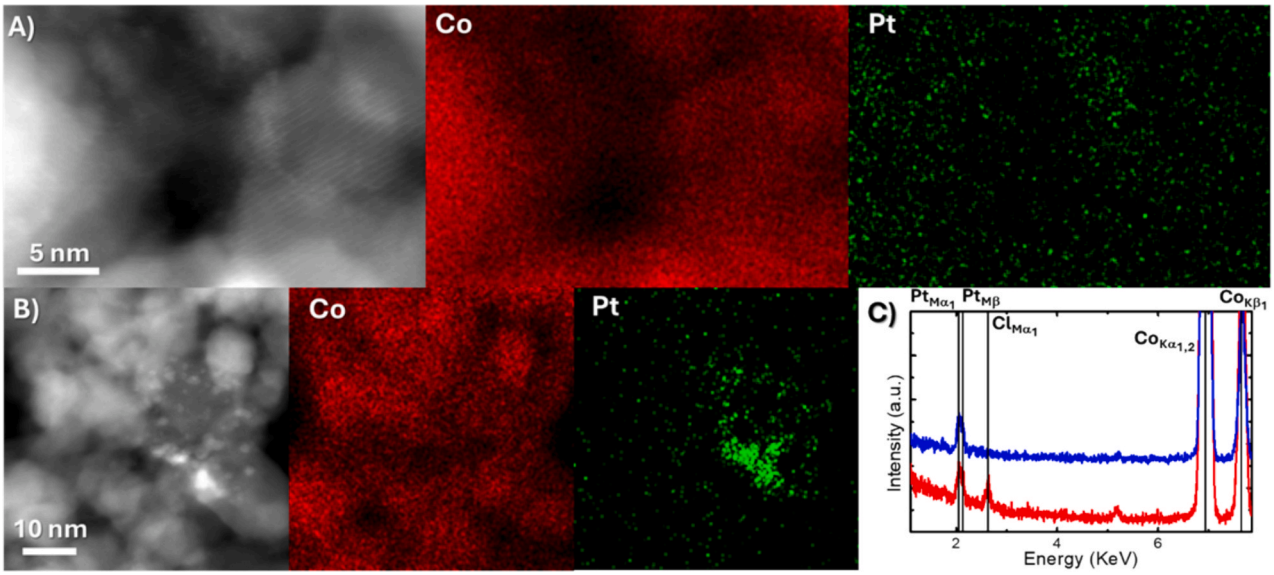

Fig. 5. Representative HAADF images and Co, Pt elemental maps of $PtCo_3O_4$ before (A) and after (B) the reaction. (C) Summed EDS spectrum of the previous element mapping experiments.

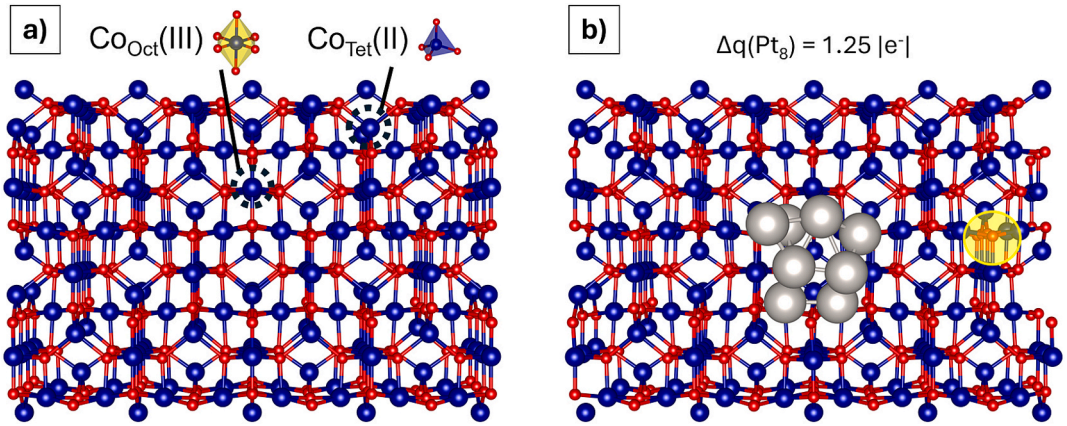

Fig. 6. Structural representation of the Co_3O_4 (1 1 0) and Pt_8/Co_3O_4 (1 1 0) models. Inset are the coordination environments of Co_{Oct}(III) and Co_{Tet}(II), and the transferred Bader charge from Pt_8 to the Co_3O_4 slab. The most favourable oxygen reduction site on Pt/Co_3O_4 is circled in yellow.

adsorption of the Pt_8 cluster revealed a favourable and robust bonding to Co_3O_4 (1 1 0), E_b of −1.43 eV/Pt atom. The Pt_8 transfer part of its charge density to the reducible oxide, $\Delta q\ (Pt_8) = 1.25\ |e^-|$, confirming the MSIs of $PtCo_3O_4$ and resembling the polarisation of the interface ($Pt^{\delta+}Co_3^{\delta-}O_4$) observed *via* the combined XPS/DRIFTS study of the surface.

Hence, to prove the impact of said MSIs on the surface redox properties, an oxygen vacancy was introduced for the non-equivalent oxygen sites of the models (Fig. S6 for the complete list of tested sites and corresponding energies). The results for the most favourable sites on a Co_3O_4 (1 1 0) slab (O^{2c} and O^{3c}), in the presence and absence of Pt, are shown in Table 1. In agreement with the literature, the thermodynamic barriers on pristine Co_3O_4 were 2.42 and 4.15 eV, respectively for the O^{3c} and O^{2c} sites [52,53]. On $PtCo_3O_4$, the transfer of charge from Pt to Co_3O_4 enhanced the oxygen mobility in the proximity of the Pt cluster compared to the pristine oxide, facilitating the formation of vacancies on both the oxygen sites. Energy barriers as low as 0.79 and 1.52 eV were found for O^{3c} and O^{2c}, respectively. The simulations proved at atomic scale that the MSIs of Pt Co_3O_4 enhanced the mobility of oxygen and that the surface redox properties of the oxide are modified by the presence of a metal/oxide interface. Furthermore, the O^{3c} sites were found as the most favourable reduction sites, and the information agreed with the decrease of octahedral Co(III) ions observed using the combined information from XPS and the quantitative XAFS data.

Table 1
Most favourable oxygen vacancy formation energy $E_f(O)$ on the Co_3O_4 (1 1 0) and Pt/Co_3O_4 (1 1 0) models.

	$E_f(O^{3c})$/eV	$E_f(O^{2c})$/eV
Co_3O_4 (1 1 0)	2.42	4.15
Pt_8/Co_3O_4 (1 1 0)	0.79	1.52

4. Conclusions

Cobalt oxide (Co_3O_4) impregnated with 1 wt% Pt ($PtCo_3O_4$) was tested in the ammonia borane dehydrogenation and compared with a $PtAl_2O_3$ reference and the pristine oxide (Co_3O_4) to disclose the influence of metal-support interactions (MSIs) on the catalysts under reaction conditions. $PtCo_3O_4$ exhibited a sigmoidal hydrogen evolution profile, which is indicative of modifications of the material, uniquely attributed to the co-presence of Pt and Co_3O_4 through a comparison with the other catalysts and recycling tests. In situ ATR-IR experiments on $PtCo_3O_4$ identified an irreversible surface reduction of Co_3O_4 through H species

abstracted from the B-H bonds of ammonia borane, and the XPS/DRIFT characterisation attributed such modifications to the presence of MSIs. The thorough characterisation of $PtCo_3O_4$ before and after the reaction highlighted the reduction and agglomeration of supported Pt and the reduction of surface Co(III) ions to Co(II) through a combination of XPS/DRIFT and STEM-HAADF data. The reduction of the support was correlated to a variation in the relative population of tetrahedral (Td) and octahedral (Oh) sites with XAS, although modifications of the long range ordering were excluded *via* XRD. The modification of the redox property of Co_3O_4 in the presence of Pt was investigated through DFT on a model Co_3O_4 (1 1 0) slab. The formation of a highly stable interface (E_{ads} of −1.43 eV/Pt atom), the Pt-to-Co_3O_4 charge transfer and the enhanced local reducibility of $PtCo_3O_4$ enhanced compared to that of pristine Co_3O_4 were correlated with the MSIs observed from the experiments. In particular, three-fold oxygen coordinated to octahedral Co (III) ions were found as the most favourable reduction sites. The entire catalyst surface is modified by the interaction with ammonia borane, and the active phase is generated *in-situ*. Overall, we shed light on the nature of the active sites for a $PtCo_3O_4$ catalyst, one of the optimal materials for the ammonia borane dehydrogenation. It is expected that these results will be useful in a dual way, to guide the design of new catalysts with improved performance, and to use ammonia borane dehydrogenation and the Finke-Watzky model to simply and indirectly track the set of interfacial changes occurring *in situ*.

Funding sources

This work was partially supported by the by the project with reference number PID2020-113809RB-C33 from the Ministry of Science, Innovation, and Universities of Spain.

CRediT authorship contribution statement

Silvio Bellomi: Writing – original draft, Conceptualization. **Daniel C. Cano-Blanco:** Investigation, Formal analysis. **Yaning Han:** Investigation, Formal analysis. **Juan J. Delgado:** Validation, Investigation. **Xiaowei Chen:** Validation, Investigation. **Kirill A. Lomachenko:** Formal analysis, Data curation. **Ilaria Barlocco:** Formal analysis, Data curation. **Davide Ferri:** Writing – review & editing, Validation. **Alberto Roldan:** Visualization, Validation. **Alberto Villa:** Writing – review & editing, Validation, Supervision.

Declaration of competing interest

The authors declare that they have no known competing financial interests or personal relationships that could have appeared to influence the work reported in this paper.

Acknowledgment

The authors acknowledge computing time on the facilities of Supercomputing Wales and the Advanced Research Computing Cardiff (ARCCA) at Cardiff University. ESRF is acknowledged for granting the beamtime at BM23 beamline (experiment MA-6214). S.B. thanks Dr. Olga Safonova for the useful discussions.

Appendix A. Supplementary data

Supplementary data to this article can be found online at https://doi.org/10.1016/j.apsusc.2025.164116.

Data availability

Data will be made available on request.

References

[1] W. Schneider, M. Heyde, H. Freund, Charge control in model catalysis: the decisive role of the oxide–nanoparticle interface, Chem. Eur. J. 24 (2018) 2317–2327.
[2] A.K. Singh, Q. Xu, Synergistic catalysis over bimetallic alloy nanoparticles, ChemCatChem 5 (2013) 652–676.
[3] A. Ruiz Puigdollers, P. Schlexer, S. Tosoni, G. Pacchioni, Increasing oxide reducibility: the role of metal/oxide interfaces in the formation of oxygen vacancies, ACS Catal. 7 (2017) 6493–6513, https://doi.org/10.1021/acscatal.7b01913.
[4] T.W. van Deelen, C. Hernández Mejía, K.P. de Jong, Control of metal-support interactions in heterogeneous catalysts to enhance activity and selectivity, Nat. Catal. 2 (2019) 955–970.
[5] A. Beck, X. Huang, L. Artiglia, M. Zabilskiy, X. Wang, P. Rzepka, D. Palagin, M.-G. Willinger, J.A. van Bokhoven, The dynamics of overlayer formation on catalyst nanoparticles and strong metal-support interaction, Nat. Commun. 11 (2020) 3220.
[6] J. Engel, E. Schwartz, C.R.A. Catlow, A. Roldan, The influence of oxygen vacancy and Ce 3+ ion positions on the properties of small gold clusters supported on CeO 2–x (111), J Mater Chem A Mater 8 (2020) 15695–15705.
[7] M. Haruta, S. Tsubota, T. Kobayashi, H. Kageyama, M.J. Genet, B. Delmon, Low-temperature oxidation of CO over gold supported on TiO2, α-Fe2O3, and Co3O4, J. Catal. 144 (1993) 175–192.
[8] M. Valden, X. Lai, D. Goodman, Onset of catalytic activity of gold clusters on titania with the appearance of nonmetallic properties, Science 281 (1998) (1979) 1647–1650.
[9] H. Song, X. Meng, Z. Wang, Z. Wang, H. Chen, Y. Weng, F. Ichihara, M. Oshikiri, T. Kako, J. Ye, Visible-light-mediated methane activation for steam methane reforming under mild conditions: a case study of Rh/TiO2 catalysts, ACS Catal. 8 (2018) 7556–7565.
[10] G. Kumar, L. Tibbitts, J. Newell, B. Panthi, A. Mukhopadhyay, R.M. Rioux, C. J. Pursell, M. Janik, B.D. Chandler, Evaluating differences in the active-site electronics of supported Au nanoparticle catalysts using Hammett and DFT studies, Nat. Chem. 10 (2018) 268–274.
[11] H. Wang, Y. Chi, D. Gao, Z. Wang, C. Wang, L. Wang, M. Wang, D. Cheng, J. Zhang, C. Wu, Enhancing formic acid dehydrogenation for hydrogen production with the metal/organic interface, Appl. Catal. B 255 (2019) 117776.
[12] P. Adamou, S. Bellomi, E. Harkou, X. Chen, J.J. Delgado, N. Dimitratos, G. Manos, A. Villa, A. Constantinou, Hydrous hydrazine decomposition over Rh/Al2O3 catalyst: experimental and CFD studies, Chem. Eng. J. (2024) 152715.
[13] S. Bellomi, D.C. Cano-Blanco, I. Barlocco, J.J. Delgado, X. Chen, L. Prati, D. Ferri, N. Dimitratos, A. Roldan, A. Villa, Probing the metal/oxide interface of IrCoCeOx in N2H4·H2O decomposition: an experimental and computational study, ACS Appl. Mater. Interfaces (2024).
[14] S. Bellomi, D. Motta, M. Stucchi, L. Prati, N. Dimitratos, A. Villa, Hydrogen production from hydrous hydrazine decomposition using Ir catalysts: effect of the preparation method and the support, Catalysts 14 (2024) 119.
[15] S. Akbayrak, Y. Tonbul, S. Özkar, Magnetically separable Rh0/Co3O4 nanocatalyst provides over a million turnovers in hydrogen release from ammonia borane, ACS Sustain. Chem. Eng. 8 (2020) 4216–4224.
[16] S. Akbayrak, Y. Tonbul, S. Özkar, Ceria supported rhodium nanoparticles: superb catalytic activity in hydrogen generation from the hydrolysis of ammonia borane, Appl. Catal. B 198 (2016) 162–170.
[17] S. Akbayrak, S. Özkar, Magnetically isolable Pt0/Co3O4 nanocatalysts: outstanding catalytic activity and high reusability in hydrolytic dehydrogenation of ammonia borane, ACS Appl. Mater. Interfaces 13 (2021) 34341–34348, https://doi.org/10.1021/acsami.1c08362.
[18] M. Chandra, Q. Xu, Room temperature hydrogen generation from aqueous ammonia-borane using noble metal nano-clusters as highly active catalysts, J. Power Sources 168 (2007) 135–142.
[19] Q. Xu, M. Chandra, A portable hydrogen generation system: catalytic hydrolysis of ammonia–borane, J. Alloy. Compd. 446 (2007) 729–732.
[20] C.Y. Alpaydın, S.K. Gülbay, C.O. Colpan, A review on the catalysts used for hydrogen production from ammonia borane, Int. J. Hydrogen Energy 45 (2020) 3414–3434.
[21] P.V. Ramachandran, H. Mistry, A.S. Kulkarni, P.D. Gagare, Ammonia-mediated, large-scale synthesis of ammonia borane, Dalton Trans. 43 (2014) 16580–16583.
[22] M.G. Hu, J.M. Van Paasschen, R.A. Geanangel, New synthetic approaches to ammonia-borane and its deuterated derivatives, J. Inorg. Nucl. Chem. 39 (1977) 2147–2150.
[23] S. Özkar, How to increase the catalytic efficacy of platinum-based nanocatalysts for hydrogen generation from the hydrolysis of ammonia borane, Int. J. Energy Res. 46 (2022) 22089–22099.
[24] J. Jiang, J. Zhang, B. Wu, S. Tu, When Pt nanoparticles meet oxygen-deficient Co3O4: enabling superior performance towards on-demand hydrogen generation from hydrolytic dehydrogenation of dimethylamine borane, J. Alloy. Compd. 969 (2023) 172369, https://doi.org/10.1016/j.jallcom.2023.172369.
[25] M. Li, S. Zhang, J. Zhao, H. Wang, Maximizing metal–support interactions in Pt/Co3O4 nanocages to simultaneously boost hydrogen production activity and durability, ACS Appl. Mater. Interfaces 13 (2021) 57362–57371, https://doi.org/10.1021/acsami.1c18403.
[26] R. Prins, Hydrogen spillover, facts and fiction, Chem. Rev. 112 (2012) 2714–2738.
[27] R. Prins, V.K. Pálfi, M. Reiher, Hydrogen spillover to nonreducible supports, J. Phys. Chem. C 116 (2012) 14274–14283.

[28] J. Pal, P. Chauhan, Study of physical properties of cobalt oxide (Co3O4) nanocrystals, Mater. Charact. 61 (2010) 575–579, https://doi.org/10.1016/j.matchar.2010.02.017.

[29] M.A. Watzky, R.G. Finke, Transition metal nanocluster formation kinetic and mechanistic studies. A new mechanism when hydrogen is the reductant: slow, continuous nucleation and fast autocatalytic surface growth, J. Am. Chem. Soc. 119 (1997) 10382–10400, https://doi.org/10.1021/ja9705102.

[30] L. Bentea, M.A. Watzky, R.G. Finke, Sigmoidal nucleation and growth curves across nature fit by the Finke–Watzky model of slow continuous nucleation and autocatalytic growth: explicit formulas for the lag and growth times plus other key insights, J. Phys. Chem. C 121 (2017) 5302–5312.

[31] J.A. Widegren, J.D. Aiken, S. Özkar, R.G. Finke, Additional investigations of a new kinetic method to follow transition-metal nanocluster formation, including the discovery of heterolytic hydrogen activation in nanocluster nucleation reactions, Chem. Mater. 13 (2001) 312–324.

[32] E. Lam, J.J. Corral-Pérez, K. Larmier, G. Noh, P. Wolf, A. Comas-Vives, A. Urakawa, C. Copéret, CO2 hydrogenation on Cu/Al2O3: role of the metal/support interface in driving activity and selectivity of a bifunctional catalyst, Angew. Chem. Int. Ed. 58 (2019) 13989–13996.

[33] M. Agote-Arán, S. Alijani, C. Coffano, A. Villa, D. Ferri, Effect of Pt particle size and phosphorous addition on furfural hydrogenation over Pt/Al2O3, Catal. Lett. (2021) 1–11.

[34] L.F. Liotta, G. Di Carlo, G. Pantaleo, G. Deganello, Co3O4/CeO2 and Co3O4/CeO2–ZrO2 composite catalysts for methane combustion: Correlation between morphology reduction properties and catalytic activity, Catal. Commun. 6 (2005) 329–336.

[35] M. Roselló-Merino, R.J. Rama, J. Díez, S. Conejero, Catalytic dehydrocoupling of amine-boranes and amines into diaminoboranes: isolation of a Pt (ii), Shimoi-type, η 1-BH complex, Chem. Commun. 52 (2016) 8389–8392.

[36] A. Telleria, P.W.N.M. van Leeuwen, Z. Freixa, Azobenzene-based ruthenium (II) catalysts for light-controlled hydrogen generation, Dalton Trans. 46 (2017) 3569–3578.

[37] O. Mathon, A. Beteva, J. Borrel, D. Bugnazet, S. Gatla, R. Hino, I. Kantor, T. Mairs, M. Muñoz, S. Pasternak, The time-resolved and extreme conditions XAS (TEXAS) facility at the European Synchrotron Radiation Facility: the general-purpose EXAFS bending-magnet beamline BM23, Synchrotron Radiation 22 (2015) 1548–1554.

[38] B. Ravel, M. Newville, ATHENA, ARTEMIS, HEPHAESTUS: data analysis for X-ray absorption spectroscopy using IFEFFIT, J. Synchrotron Radiat. 12 (2005) 537–541.

[39] T. Bürgi, R. Wirz, A. Baiker, In situ attenuated total reflection infrared spectroscopy: a sensitive tool for the investigation of reduction− oxidation processes on heterogeneous Pd metal catalysts, J. Phys. Chem. B 107 (2003) 6774–6781.

[40] C.J. Baranowski, T. Fovanna, M. Roger, M. Signorile, J. McCaig, A.M. Bahmanpour, D. Ferri, O. Krocher, Water inhibition of oxymethylene dimethyl ether synthesis over zeolite H-Beta: a combined kinetic and in situ ATR-IR study, ACS Catal. 10 (2020) 8106–8119.

[41] S. Campisi, D. Ferri, A. Villa, W. Wang, D. Wang, O. Kröcher, L. Prati, Selectivity control in palladium-catalyzed alcohol oxidation through selective blocking of active sites, J. Phys. Chem. C 120 (2016) 14027–14033, https://doi.org/10.1021/acs.jpcc.6b01549.

[42] D. Baurecht, U.P. Fringeli, Quantitative modulated excitation Fourier transform infrared spectroscopy, Rev. Sci. Instrum. 72 (2001) 3782–3792.

[43] G. Kresse, J. Furthmüller, Efficient iterative schemes for ab initio total-energy calculations using a plane-wave basis set, Phys. Rev. B: Condens. Matter Mater. Phys. 54 (1996) 11169–11186, https://doi.org/10.1103/PhysRevB.54.11169.

[44] G. Kresse, D. Joubert, From ultrasoft pseudopotentials to the projector augmented-wave method, Phys. Rev. B 59 (1999) 1758–1775, https://doi.org/10.1103/PhysRevB.59.1758.

[45] B. Hammer, L.B. Hansen, J.K. Nørskov, Improved adsorption energetics within density-functional theory using revised Perdew-Burke-Ernzerhof functionals, Phys. Rev. B 59 (1999) 7413–7421, https://doi.org/10.1103/PhysRevB.59.7413.

[46] J.D. Pack, H.J. Monkhorst, "special points for Brillouin-zone integrations"-a reply, Phys. Rev. B 16 (1977) 1748–1749, https://doi.org/10.1103/PhysRevB.16.1748.

[47] S.L. Dudarev, G.A. Botton, S.Y. Savrasov, C.J. Humphreys, A.P. Sutton, Electron-energy-loss spectra and the structural stability of nickel oxide: an LSDA+U study, Phys. Rev. B 57 (1998) 1505–1509, https://doi.org/10.1103/PhysRevB.57.1505.

[48] A. Cadi-Essadek, A. Roldan, D. Santos-Carballal, P.E. Ngoepe, M. Claeys, N.H. de Leeuw, DFT+ U study of the electronic, magnetic and mechanical properties of Co, CoO, and Co3O4, S. Afr. J. Chem. 74 (2021) 8–16.

[49] J.-X. Liu, Y. Su, I.A.W. Filot, E.J.M. Hensen, A linear scaling relation for CO oxidation on CeO2-supported Pd, J. Am. Chem. Soc. 140 (2018) 4580–4587.

[50] A.H. Larsen, J.J. Mortensen, J. Blomqvist, I.E. Castelli, R. Christensen, M. Dułak, J. Friis, M.N. Groves, B. Hammer, C. Hargus, The atomic simulation environment—a Python library for working with atoms, J. Phys. Condens. Matter 29 (2017) 273002.

[51] X.L. Xu, J.Q. Li, DFT studies on H2O adsorption and its effect on CO oxidation over spinel Co3O4 (110) surface, Surf. Sci. 605 (2011) 1962–1967.

[52] J. Chen, A. Selloni, Electronic states and magnetic structure at the Co 3 O 4 (110) surface: a first-principles study, Phys. Rev. B—Condensed Matter Mater. Phys. 85 (2012) 85306.

[53] S. Selcuk, A. Selloni, DFT+ U study of the surface structure and stability of Co3O4 (110): dependence on U, J. Phys. Chem. C 119 (2015) 9973–9979.

[54] D. Jiang, S. Dai, The role of low-coordinate oxygen on Co 3 O 4 (110) in catalyticCO oxidation, PCCP 13 (2011) 978–984.

[55] D. Santos-Carballal, A. Roldan, R. Grau-Crespo, N.H. de Leeuw, A DFT study of the structures, stabilities and redox behaviour of the major surfaces of magnetite Fe 3 O 4, PCCP 16 (2014) 21082–21097.

[56] D. Santos-Carballal, A. Roldan, N.H. de Leeuw, Early oxidation processes on the greigite Fe3S4 (001) surface by water: a density functional theory study, J. Phys. Chem. C 120 (2016) 8616–8629.

[57] S. Bellomi, I. Barlocco, X. Chen, J.J. Delgado, R. Arrigo, N. Dimitratos, A. Roldan, A. Villa, Enhanced stability of sub-nanometric iridium decorated graphitic carbon nitride for H2 production upon hydrous hydrazine decomposition, PCCP 25 (2023) 1081–1095.

[58] J. Engel, S. Francis, A. Roldan, The influence of support materials on the structural and electronic properties of gold nanoparticles–a DFT study, PCCP 21 (2019) 19011–19025.

[59] J.D. Pack, H.J. Monkhorst, Special points for Brillouin-zone integrations, Phys. Rev. B 16 (1977) 1748–1749, https://doi.org/10.1103/PhysRevB.16.1748.

[60] S. Akbayrak, S. Tanyıldızı, İ. Morkan, S. Özkar, Ruthenium(0) nanoparticles supported on nanotitania as highly active and reusable catalyst in hydrogen generation from the hydrolysis of ammonia borane, Int. J. Hydrogen Energy 39 (2014) 9628–9637, https://doi.org/10.1016/j.ijhydene.2014.04.091.

[61] J.G. Cook, M.P. Van Der Meer, The optical properties of sputtered Co3O4 films, Thin Solid Films 144 (1986) 165–176.

[62] I.G. Austin, B.D. Clay, C.E. Turner, Optical absorption of small polarons in semiconducting NiO and CoO in the near and far infra-red, J. Phys. C Solid State Phys. 1 (1968) 1418.

[63] D. Gallant, M. Pézolet, S. Simard, Optical and physical properties of cobalt oxide films electrogenerated in bicarbonate aqueous media, J. Phys. Chem. B 110 (2006) 6871–6880, https://doi.org/10.1021/jp056689h.

[64] A. Paolone, F. Teocoli, S. Sanna, O. Palumbo, T. Autrey, Temperature dependence of the infrared spectrum of ammonia borane: librations, rotations, and molecular vibrations, J. Phys. Chem. C 117 (2013) 729–734.

[65] C.-C. Chou, D.-J. Lee, B.-H. Chen, Hydrogen production from hydrolysis of ammonia borane with limited water supply, Int. J. Hydrogen Energy 37 (2012) 15681–15690, https://doi.org/10.1016/j.ijhydene.2012.05.108.

[66] B. Yildirim, H. Riesen, Coordination and oxidation state analysis of cobalt in nanocrystalline LiGa5O8 by X-ray absorption spectroscopy, J. Phys. Conf. Ser. IOP Publishing (2013) 12011.

[67] M. Risch, F. Ringleb, M. Kohlhoff, P. Bogdanoff, P. Chernev, I. Zaharieva, H. Dau, Water oxidation by amorphous cobalt-based oxides: in situ tracking of redox transitions and mode of catalysis, Energy Environ. Sci. 8 (2015) 661–674.

[68] Q. Yang, P. Cui, Q. Ye, S. Chen, Z. Wu, X-ray absorption study of the geometry structure of Co2+/Co3+ in ammonia solution, J. Mol. Struct. 1098 (2015) 306–310, https://doi.org/10.1016/j.molstruc.2015.06.034.

[69] J. Huang, H. Sheng, R.D. Ross, J. Han, X. Wang, B. Song, S. Jin, Modifying redox properties and local bonding of Co3O4 by CeO2 enhances oxygen evolution catalysis in acid, Nat. Commun. 12 (2021) 3036.

[70] B. Ouyang, S. Xiong, Y. Zhang, B. Liu, J. Li, The study of morphology effect of Pt/Co3O4 catalysts for higher alcohol synthesis from CO2 hydrogenation, Appl. Catal. A 543 (2017) 189–195, https://doi.org/10.1016/j.apcata.2017.06.031.